

Article

Synergistic Effect of Co and Ni Co-Existence on Catalytic Decomposition of Ammonia to Hydrogen – Effect of Catalytic Support and Mg-Al Oxide Matrix

Andrzej Kowalczyk *, Małgorzata Rutkowska, Sylwia Gnyła, Michał Pacia and Lucjan Chmielarz *

Faculty of Chemistry, Jagiellonian University, Gronostajowa 2, 30-387 Kraków, Poland; malgorzata.rutkowska@uj.edu.pl (M.R.); sylwia.gnyla@student.uj.edu.pl (S.G.); pacia@chemia.uj.edu.pl (M.P.)

* Correspondence: andrzej.kowalczyk@uj.edu.pl (A.K.); lucjan.chmielarz@uj.edu.pl (L.C.)

Abstract: Hydrotalcite-derived mixed metal oxides containing Co and Ni and containing these metals supported on MgO and Al₂O₃ were prepared and tested as catalysts for the decomposition of ammonia to hydrogen and nitrogen. The obtained samples were characterised in terms of chemical composition (ICP-OES), structure (XRD), textural parameters (low-temperature N₂ adsorption-desorption, SEM), form and aggregation of transition-metal species (UV-Vis DRS), reducibility (H₂-TPR) and surface acidity (NH₃-TPD). The catalytic efficiency of the tested systems strongly depends on the support used. Generally, the alumina-based catalyst operated at lower temperatures compared to transition metals deposited on MgO. For both series of catalysts, a synergistic effect of the co-existence of cobalt and nickel on the catalytic efficiency was observed. The best catalytic results were obtained for hydrotalcite-derived catalysts; however, in the case of these catalysts, an increase in the Al/Mg ratio resulted in a further increase in catalytic activity in the decomposition of ammonia.

Keywords: hydrogen; ammonia decomposition; hydrotalcite

Citation: Kowalczyk, A.; Rutkowska, M.; Gnyła, S.; Pacia, M.; Chmielarz, L. Synergistic Effect of Co and Ni Co-Existence on Catalytic Decomposition of Ammonia to Hydrogen – Effect of Catalytic Support and Mg-Al Oxide Matrix. *ChemEngineering* **2024**, *8*, 55. <https://doi.org/10.3390/chemengineering8030055>

Academic Editor: Lidia Pino

Received: 15 February 2024

Revised: 11 May 2024

Accepted: 21 May 2024

Published: 24 May 2024



Copyright: © 2024 by the authors. Licensee MDPI, Basel, Switzerland. This article is an open access article distributed under the terms and conditions of the Creative Commons Attribution (CC BY) license (<https://creativecommons.org/licenses/by/4.0/>).

1. Introduction

Today, renewable energy and sustainability are the most important issues in strategies for the development of new technologies. Depletion of fossil-fuel resources, as well as the emission of carbon dioxide and other pollutants due to their use, have led to a growing interest in hydrogen as a clean energy source in zero-emission vehicles, energy production, and various industrial applications [1]. The problem of hydrogen sustainability is dependent on the method used for its production, especially on the energy source used for its generation. When energy from fossil fuels is used, the product is called grey hydrogen. On the other hand, production of so-called green hydrogen is based on, e.g., splitting water into hydrogen and oxygen by using electricity obtained from renewable sources and other methods that do not use fossil fuels. For the moment, green hydrogen is very costly to produce in large quantities, an important issue that limits its production and usage. Another important problem is related to hydrogen storage and transportation to end users [2]. The low volumetric density of hydrogen hinders its transport on a global scale, as well as its large-scale storage [3]. Two methods of hydrogen storage are used: physical hydrogen storage (high-pressure and liquid hydrogen storage, as well as cryo-compressed hydrogen storage) [4] and chemical hydrogen storage (e.g., metal hydrides, liquid organic hydrogen carriers and metal-organic frameworks) [5]. Ammonia, due to its properties, is a very promising chemical hydrogen carrier. Ammonia is characterized by a high hydrogen content (17.8%) and can be liquefied relatively easily at low pressure (8.6 bar) and temperature (20 °C) [6,7]. Hydrogen can be recovered from ammonia by its thermal decomposition, which requires a high operation temperature and therefore

additional costs. The temperature at which ammonia decomposes to hydrogen and nitrogen can be significantly decreased by using catalysts. Ruthenium-containing systems were identified as active catalysts for ammonia decomposition, operating effectively at temperatures below 450 °C [8]; however, commercial-scale application is difficult due to the high cost of ruthenium [9]. Many efforts have been made to decrease the cost of Ru-based catalysts, including dispersing metal nanoparticles on various supports and limiting the ruthenium loading in catalytic systems. However, such catalysts cannot meet the demands needed to scale up the process, mainly due to incomplete ammonia conversion at lower temperatures, insufficient stability, and still-high costs [10,11]. Therefore, the search for non-ruthenium catalysts with high activity, high stability, and low cost has attracted significant attention from scientists and engineers. Co- and Ni-based catalysts have been reported to be the most promising alternatives to Ru-based ones [12–15]. The very important role of supports used for cobalt and nickel deposition in determining the efficiency of ammonia decomposition has been reported [12–15]. The supports may increase the density of active centres, influence the dispersion of metal nanoparticles and their stability and may modify surface chemistry to facilitate the diffusion of intermediate species under reaction conditions [16]. The mechanism of catalytic decomposition of ammonia includes dissociative adsorption of ammonia, relatively fast recombination and desorption of H₂ and much slower recombination and desorption of N₂ molecules, which is considered the rate-determining step [17]. It is postulated that the binding energy between metal and nitrogen (M-N) determines the catalytic activity of ammonia decomposition [15]. In the case of an M-N binding energy that is too weak, ammonia desorption is more likely than its dehydrogenation and the efficiency of ammonia decomposition is therefore low. On the other hand, a too-strong M-N binding energy is suitable for dissociative adsorption of ammonia but it is unfavorable for recombination of N atoms and desorption of N₂ molecules. Recombination of N atoms has also been attributed to the size of metal species dispersed on the support surface, especially at the metal–support interfaces where the recombination process is postulated to occur [14]. Thus, the selection of catalytically active metal components, as well as the appropriate support, is a crucial issue in designing catalysts for ammonia decomposition.

In the presented studies, the catalytic performance of monometallic cobalt and nickel catalysts, as well as those of bimetallic Co-Ni catalysts supported on MgO and Al₂O₃ and hydrotalcite-derived mixed metal oxides of the types Co-Mg-Al-O, Ni-Mg-Al-O and Co-Ni-Mg-Al-O, was verified. The roles of the catalytic support and catalyst compositions are presented and discussed in relation to their catalytic activity.

2. Materials and Methods

2.1. Catalysts Preparation

Two series of hydrotalcite-like materials with metal cation molar ratios (M²⁺/M³⁺) of 1.5 and 4.0 and intended total content of Co and Ni of 5.4% were prepared. In both series, the assumed molar ratios of Co/Ni/Mg/Al were as follows: 4.0/0/76/20 (Co-HT20), 2.0/2.0/76/20 (CoNi-HT20), 0/4.0/76/20 (Ni-HT20), 4.2/0/55.8/40 (Co-HT40), 2,1/2.1/55.8/40 (CoNi-HT40) and 0/4.2/55.8/40 (Ni-HT40). Hydrotalcite-like materials were prepared by the co-precipitation method. A typical synthesis proceeded as follows: aqueous solutions of the mixed metal nitrates Mg(NO₃)₂·6H₂O (Honeywell, Germany), Al(NO₃)₃·9H₂O (ChemPur, Piekary Śląskie, Poland), Co(NO₃)₂·6H₂O (Honeywell, Germany) and Ni(NO₃)₂·6H₂O (Honeywell, Germany) were prepared in an appropriate molar ratio of components and a total metal ion concentration of 0.5 mol/L. As a precipitating agent, a 1.0 mol/L solution of NaOH (Honeywell, Germany) was used. The solution of nitrates was dropwise added to an intensively stirred solution of Na₂CO₃ (0.1 mol/L, POCH/Avantor, Gliwice, Poland). A constant pH of 10.0 ± 0.2 was maintained by the addition of NaOH solution. The obtained suspension was aged at 60 °C for the next 2 h with vigorous stirring, separated by filtration, washed with warm distilled water and dried overnight in air

at 60 °C. The obtained solid samples were calcined in an air atmosphere at 600 °C for 12 h.

Moreover, two series of supported catalysts containing Co and Ni with the same intended content as in hydrotalcite-like materials were prepared. Cobalt and nickel were deposited on the MgO (M) and Al₂O₃ (A) supports by incipient wetness impregnation resulting in Co-M, CoNi-M, Ni-M and Co-A, CoNi-A, Ni-A samples, respectively. The supported catalysts were obtained as follows: aqueous solutions of Co(NO₃)₂·6H₂O (Honeywell) or Ni(NO₃)₂·6H₂O (Honeywell) were prepared. Their concentrations depended on the desired metal or metals loading in the samples and the sorption volume of the supports (determined for water, which was used as a solvent). Then, MgO (Sigma-Aldrich) and Al₂O₃ (Merck KGaA, Germany) were impregnated with the appropriate volume of solution. In the next step, the samples were dried at 60 °C for 12 h and finally calcined in an air atmosphere at 600 °C for 12 h.

2.2. Catalyst Characterization

The chemical compositions of the catalysts were analysed using the inductively coupled plasma optical emission spectroscopy method (ICP-OES) with an iCAP 7400 instrument (Thermo Fisher Scientific, Waltham, MA, USA). Before analysis, catalyst samples were digested in a solution composed of 6 mL of HNO₃ (67–69%, Honeywell, Charlotte, NC, USA) and 2 mL of H₂O₂ (30%, Avantor/POCH, Gliwice, Poland). The digestion process was carried out at 190 °C using an Ethos Easy microwave digestion system (Milestone, Sorisole, Italy).

The structure of the samples was analysed using the X-ray method. Powder diffractograms were recorded by a Bruker D2 Phaser diffractometer using Cu K α radiation (λ = 0.154 nm) (Bruker, Billerica, MA, USA). The diffractograms were recorded in the 2 θ angle range of 5–70° with a step of 0.02°. Counting times of 1 s per step were used, and all samples were rotated at 15 rpm during the XRD measurements.

The specific surface area and pore volume of the catalysts were determined by low-temperature (−196 °C) nitrogen adsorption and desorption measurements using a 3Flex (Micromeritics, Norcross, GA, USA) adsorption analyser. The samples, prior to the analysis, were degassed under vacuum (0.2 mbar) at 350 °C for 24 h. The specific surface area (S_{BET}) of the catalysts was calculated using the Brunauer–Emmett–Teller (BET) model.

The form and aggregation of transition-metal species in the catalysts were verified by UV-Vis DR spectroscopy using an Evolution 220 (Thermo Scientific, Waltham, MA, USA) spectrophotometer equipped with the integrating sphere ISA-220 operating in reflectance mode. Spectra were recorded in the range 190–800 nm with a resolution of 1 nm.

Temperature-programmed reduction of catalysts with hydrogen (H₂-TPR) was done in a fixed-bed quartz flow microreactor system connected directly to a thermal conductivity detector—TCD (TCD3, Valco, Houston, TX, USA) via a heated line. Before the H₂-TPR experiment, 100 mg of the catalyst sample was placed in the microreactor and degassed in a high purity Ar (99.999%) flow at 550 °C for 30 min. In the next step, the microreactor was cooled to 50 °C, then the sample was reduced in a flow (10 mL/min) of gas mixture containing 5.0 mol% H₂ diluted in Ar (purity of both 99.999%), in a temperature range of 50–950 °C with a heating rate of 10 °C/min. The water generated during the reduction was removed from the gases by a cold trap located downstream of the microreactor.

The dispersion of metals was determined by pulse H₂ chemisorption using a microreactor system. The 100 mg sample was placed in a microreactor and reduced in a flow of 5 mol% H₂ diluted in Ar (10 mL/min). In the next step, the microreactor was cooled to 50 °C and then flushed with pure argon flow in a linear temperature programme of 50–400 °C to remove residual hydrogen from the sample surface. After the sample was cooled to 100 °C in a flow of argon, the pulses of hydrogen (0.5 mL loop, 5.0 mol% H₂ diluted in Ar) were injected into microreactor. Hydrogen consumption was monitored by the TCD detector (TCD3, Valco, Houston, TX, USA). Surface acidity (relative strength and concentration of acid sites) of the catalysts was analysed by temperature-programmed ammonia

desorption (NH₃-TPD). Experiments were performed in a flow quartz microreactor system that was connected, via heated line, directly to a quadrupole mass spectrometer (UMS TDS; PREVAC, Rogów, Poland)—that was used as a detection system. Mass flow controllers (Brooks Instrument, Hatfield, PA, USA) were used to adjust and control a flow rates of the gases used. The catalyst (100 mg) placed in the microreactor was outgassed in a flow of pure helium at 550 °C for 30 min. Then, after the microreactor was cooled to 70 °C, the sample was saturated in a flow of a certified commercial gas mixture of 1.0 mol% NH₃ diluted in helium with a flow rate of 20 mL/min for approximately 2 h. Next, to remove ammonia physisorbed on the samples, the microreactor was purged in a pure helium flow until a constant baseline level ($m/z = 16$) was attained. NH₃-TPD runs were carried out with a linear heating rate of 10 °C/min in a flow (20 mL/min) of pure helium. Calibration of the QMS detector with the certified commercial gas mixture allowed recalculation of the detector signal to determine the ammonia-desorption rate.

SEM images were taken with a Helios 5 Hydra CX PFIB microscope (Thermo Fisher Scientific, Waltham, MA, USA). Images were obtained with ETD detector working in SE mode. The accelerating voltage was set to 2 kV. Samples were placed on a carbon tape to achieve proper fixation and electric contact.

2.3. Catalytic Studies

The obtained samples were studied as catalysts for the decomposition of ammonia (DeNH₃) in a temperature range of 250–800 °C with a space velocity of 300 mL/(h·g_{cat}). The procedure for the catalytic test was as follows: 100 mg of the calcined sample (catalyst fraction size 100–160 μm) was placed in a fixed-bed flow quartz microreactor. Next, the catalyst was reduced in a flow of gas mixture containing 5.0 mol% H₂ diluted in Ar (purity of both 99.999%) at 800 °C for 12 h. Then, the reduced sample was cooled to 200 °C in a pure helium flow. The catalytic test was carried out with a linear heating rate of 10 °C/min under atmospheric pressure. The gas mixture, which contained 1.0 mol% NH₃ diluted in helium (purity of both 99.999%), was supplied to the microreactor with a flow rate of 50 mL/min. The progress of the catalytic reaction was monitored by a quadrupole mass spectrometer (UMS TDS; PREVAC, Rogów, Poland).

For the selected catalyst, an isothermal stability test was performed at 500 °C for 12 h. In an approach similar to that used in the polythermal tests, prior to the catalytic run, the catalyst was reduced (H₂/Ar, 800 °C, 12 h). The reaction was carried out in a flow of 1.0 mol% NH₃ diluted in helium (50 mL/min). The reaction's progress was monitored by a quadrupole mass spectrometer (UMS TDS; PREVAC, Rogów, Poland).

3. Results

The chemical composition, determined by the ICP-OES method, and the specific surface area of the samples, determined by low-temperature nitrogen adsorption, are compared in Table 1.

Table 1. The chemical composition, specific surface area and crystallite size.

Sample Name	S _{BET} , m ² /g	Chemical Composition, %				TM Cryst. Size ² , nm
		Mg	Al	Co	Ni	
MgO	41 (33) ¹					
Co-M	94	54.85	-	5.41	-	17.3
CoNi-M	87	54.85	-	2.69	2.74	20.6
Ni-M	74	54.88	-	-	5.68	14.8
γ-Al ₂ O ₃	132 (120) ¹					
Co-A	122	-	47.49	5.50	-	10.6
CoNi-A	124	-	48.08	2.76	2.79	10.4
Ni-A	121	-	47.18	-	5.68	13.3

HT20	174 (167) ¹					
Co-HT20	269	41.87	12.32	5.41	-	6.7
CoNi-HT20	251	41.88	12.27	2.69	2.74	7.1
Ni-HT20	272	42.06	12.29	-	5.44	4.7
HT40	205 (162) ¹					
Co-HT40	284	30.35	22.21	5.47	-	n.d.
CoNi-HT40	287	30.30	22.25	2.70	2.74	6.5
Ni-HT40	290	30.08	22.72	-	5.45	8.8

¹ The S_{BET} values determined for materials calcined at 800 °C are presented in parenthesis. ² The crystallite size was calculated on the basis of characteristic diffraction lines with the use of the Debye-Scherrer equation.

The content of the transition metals—cobalt and nickel separately and both cobalt and nickel in the bimetallic samples—is in the range of 5.41–5.68 wt.% (Table 1), indicating their very similar loadings in the studied catalysts. The specific surface area (S_{BET}) values, determined for the samples calcined at 600 °C and shown in Table 1, are significantly higher for the hydrotalcite-derived materials compared to MgO and $\gamma\text{-Al}_2\text{O}_3$. Interestingly, the calcined hydrotalcite-like samples containing transition metals presented a higher specific surface area compared to the calcined Mg-Al hydrotalcites without transition metals. The deposition of cobalt or nickel on $\gamma\text{-Al}_2\text{O}_3$ decreased its specific surface area by approximately 10%, while in the case of MgO, a significant increase in S_{BET} was observed after transition-metal deposition. This interesting effect could be explained by the formation of transition-metal-oxide aggregates on the MgO surface, which possibly contribute to the increased surface area of the catalysts. The specific surface area was also determined for the MgO and $\gamma\text{-Al}_2\text{O}_3$ supports, as well as for the calcined Mg-Al hydrotalcites at 800 °C (Table 1, values in parentheses). The S_{BET} values of the samples calcined at 800 °C are lower than those determined for materials thermally treated at 600 °C. In the case of MgO and HT40, the specific surface area decreased by about 20%, while for $\gamma\text{-Al}_2\text{O}_3$ and HT20, it decreased by 9 and 4%, respectively.

The structure of the catalytic materials was analysed by the X-ray diffraction method. Figure 1 presents diffractograms recorded for the catalytic supports $\gamma\text{-Al}_2\text{O}_3$ and MgO, as well as for these supports after modification with cobalt and nickel deposited by the impregnation method. Apart from the characteristic diffraction peaks of alumina [18] and magnesium oxides [19], no other reflections were found. The deposition of cobalt on $\gamma\text{-Al}_2\text{O}_3$ followed by calcination at 600 °C resulted in the appearance of new reflections characteristic of CoO [20] and spinel phases, possibly Co_3O_4 or CoAl_2O_4 [21]. Neither the formation of NiO, nor that of any spinel phases, was detected for nickel-modified alumina support [22]. Simultaneous deposition of cobalt and nickel into $\gamma\text{-Al}_2\text{O}_3$, in a process similar to that seen for the sample modified with cobalt, resulted in new diffraction peaks at positions characteristic of the CoO and spinel phases. Significant changes were observed in the diffractograms of the samples reduced in hydrogen flow at 800 °C (Figure 1A). In the case of the Ni-A and Co-A samples, the characteristic reflections of metallic nickel [23] and cobalt [24] were identified. The intensity of the characteristic reflections of nickel is significantly higher compared to that of the reflections representing metallic cobalt. The positions of these reflections in diffractograms of the sample containing both nickel and cobalt, CoNi-A, are between the characteristic diffraction peaks of metallic nickel and cobalt in the diffractograms of Ni-A and Co-A, respectively (Figure 1A), indicating the formation of bimetallic Ni-Co crystallites. The structure of $\gamma\text{-Al}_2\text{O}_3$ was not destroyed by thermal treatment in a hydrogen flow at 800 °C.

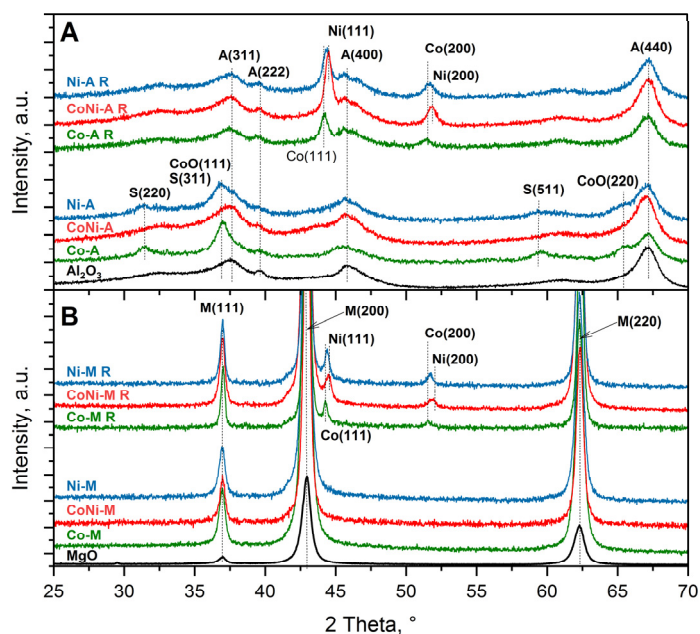


Figure 1. XRD diffraction patterns of catalysts supported on γ -Al₂O₃ (A) and MgO (B). Samples reduced in hydrogen at 800 °C are marked 'R'.

The diffractogram recorded for the MgO support is characterised by peaks typical of magnesium oxide diffraction [19]. Any new reflections were observed after deposition of nickel, cobalt or both these metals on MgO, followed by calcination at 600 °C (Figure 1B). However, the reduction of these samples in a hydrogen flow at 800 °C resulted in the appearance of new diffraction peaks characteristic of metallic nickel (Ni-M) [23] and cobalt (Co-M) [24]. The appropriate diffraction peaks recorded for the CoNi-M sample are located between the positions characteristic of metallic nickel and cobalt. Thus, the formation of bimetallic Ni-Co crystallites is supposed in the case of the CoNi-M sample (Figure 1B).

The third series of catalysts was obtained by synthesis of hydrotalcite-like samples containing, apart from magnesium and aluminium, various contents of nickel, cobalt, or both of these metals. The diffractograms recorded for these samples prove that their structure is characteristic of hydrotalcite-like materials (Figure 2A,B). Beyond the characteristic reflections of the hydrotalcite structure [25], no other diffraction peaks were found, indicating the high phase purity of the obtained samples. Calcination of hydrotalcite-like samples at 600 °C resulted in their thermal decomposition into mixed metal-oxide systems (Figure 2C,D). In diffractograms of samples with the lower Al/Mg ratio (HT20 series), only reflections characteristic of periclase [26] could be identified. For samples with the higher Al/Mg ratio (HT40 series), additional broad reflections characteristic of NiO [27] and CoO [28] were detected. Thus, it seems that segregation of the transition-metal oxides under calcination conditions is more privileged in the Mg-Al oxide matrix with higher alumina content. Reduction of hydrotalcite-derived samples in a hydrogen flow at 800 °C resulted in the appearance of diffraction peaks characteristic of metallic nickel [23]. Any reflections indicating metallic cobalt were found in the diffractogram of the reduced Co-HT20 sample, while in the case of Co-HT40, only a shoulder at 44°, possibly assigned to the plane (111) of metallic cobalt, was identified [24] (Figure 2C,D). Thus, the formation of metallic nickel crystallites is more privileged than the formation of metallic cobalt crystallites. The position of the metallic nickel reflections in diffractograms of CoNi-HT20 and CoNi-HT40 is slightly shifted to lower values of 2 theta angles compared to Ni-HT20 and Ni-HT40. Thus, the formation of bimetallic Ni-Co crystallites also cannot be excluded in this series

metal-oxide aggregates. Possibly, they are much better dispersed and are partially occluded in the MgO-Al₂O₃ matrix.

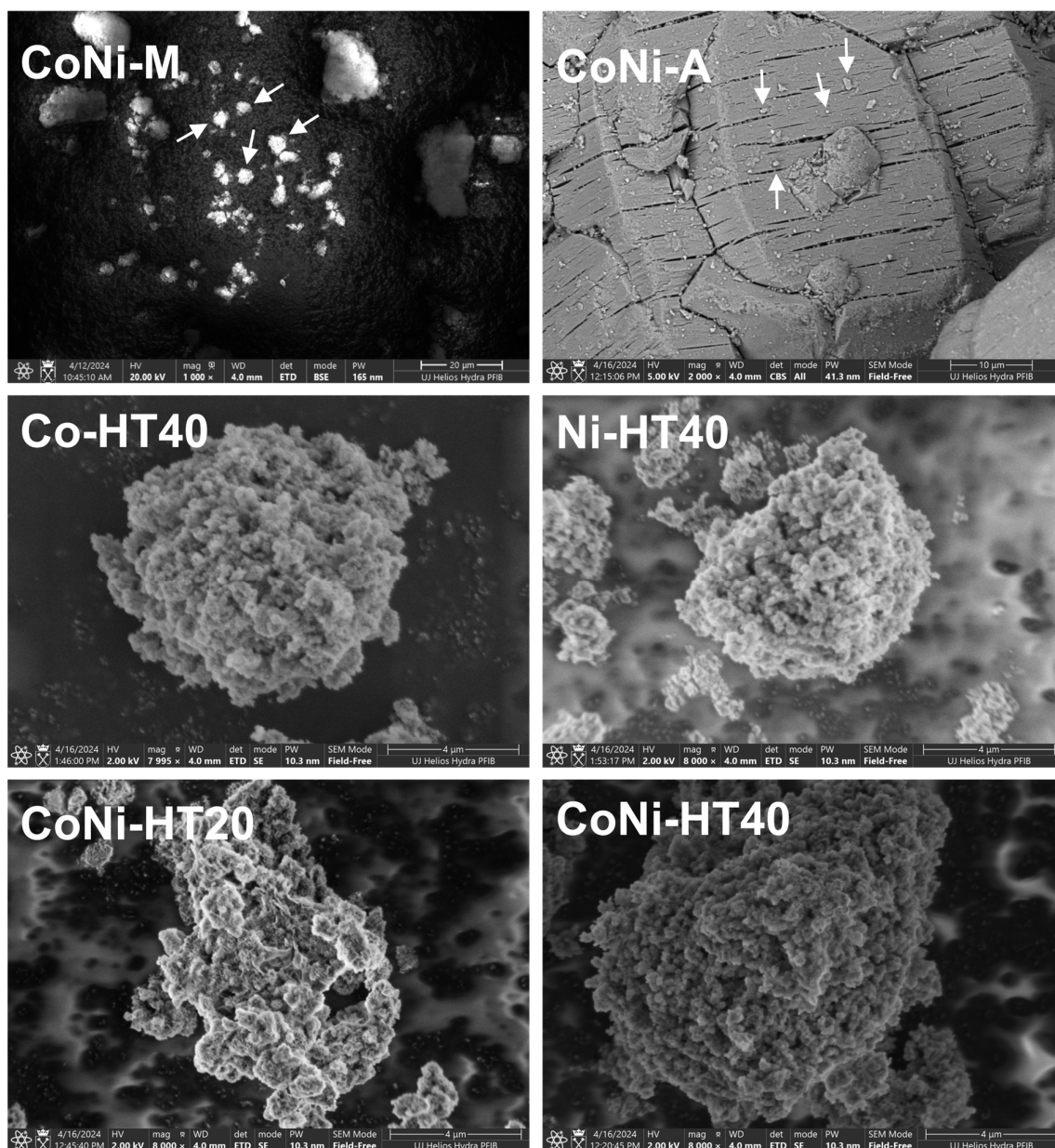


Figure 3. SEM images of the samples supported on MgO (CoNi-M) and γ -Al₂O₃ (CoNi-A) (white arrows indicate metal oxide aggregates on the support surface) as well as hydrotalcite-derived catalysts of HT20 (CoNi-HT20) and HT40 (Co-HT40, CoNi-HT40 and Ni-HT40) series.

Table 2. Hydrogen consumption during sample reduction, degree of metal reduction, surface content of metals and their dispersion on the sample surface, metal-particle diameter and TOF.

Sample Name	H ₂ Consum. ¹ , μmol/g	Reduction Degree ² , %	Moles of Metal on the Sample Surface ³ , μmol/g	Metal Dispersion ³ , %	Metal Particle Diameter ⁴ , nm	TOF at 500 °C, 1/s
Co-M	193.0	21.0	-	-	-	-
CoNi-M	212.5	23.0	6.26	0.66	2730	0.83
Ni-M	220.9	22.8	-	-	-	-

Co-A	532.9	57.1	-	-	-	-
CoNi-A	520.7	55.2	24.28	2.57	700	1.05
Ni-A	480.8	49.7	-	-	-	-
Co-HT20	275.2	30.0	-	-	-	-
CoNi-HT20	287.1	31.1	-	-	-	-
Ni-HT20	253.7	26.2	-	-	-	-
Co-HT40	361.4	38.9	48.84	5.26	345	0.64
CoNi-HT40	544.5	58.9	66.39	7.18	255	0.50
Ni-HT40	515.0	55.5	95.68	10.30	175	0.32

¹ Determined by TPR profiles from 100 °C to 950 °C. Reference gas mixture 5.0 mol% H₂/Ar was used to calibrate the TCD signal. ² In relation to the total metal content. ³ Determined by pulse H₂ chemisorption at 100 °C. ⁴ Calculation of the average particle size of assuming their spherical shape.

The form and aggregation of transition metals in catalysts was analysed by UV-VIS DRS studies (Figure 4). The spectrum recorded for Al₂O₃ not modified with transition metals was characterised by a broad band centred at approximately 255 nm (Figure 4A) associated with electronic-charge transfer and with the accumulation of defects in the structure of this material [29]. In a spectrum of Ni-A, the absorption band at around 380 nm is assigned to octahedrally coordinated Ni²⁺ cations. The band at about 600 nm corresponds to the tetrahedral Ni²⁺ cations in the NiAl₂O₄ spinel, whereas that around 635 nm is due to the d-d transition of octahedral Ni²⁺ in Ni-oxides [30–34]. Thus, besides the nickel in NiO, there is also a significant contribution of nickel in the spinel phase formed by the interaction of deposited metal with the alumina support.

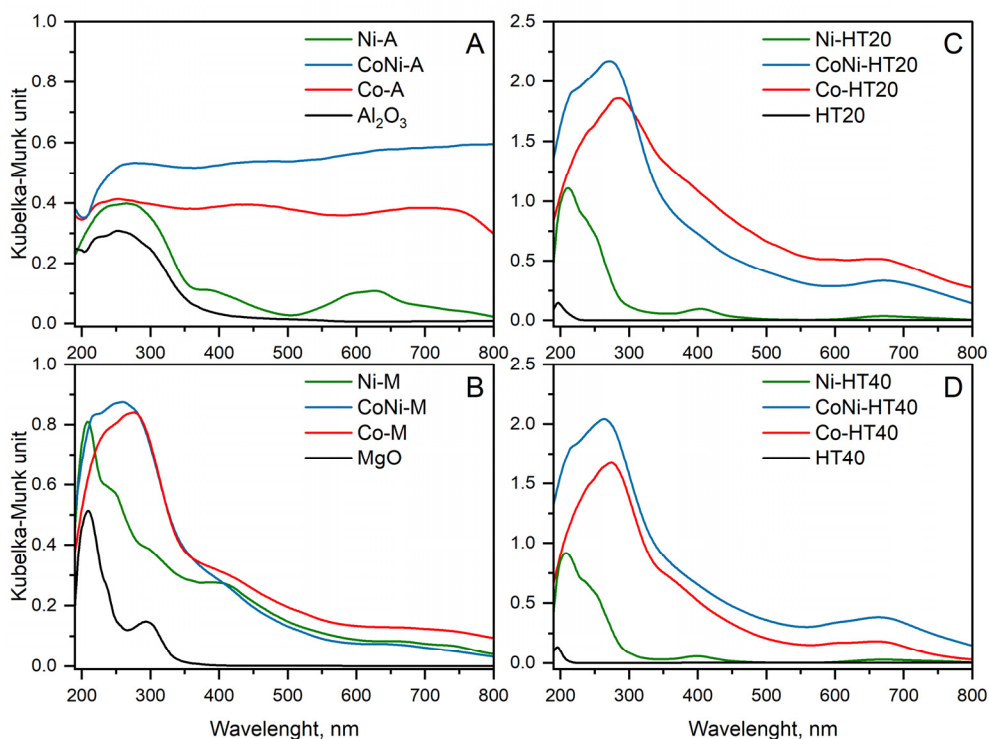


Figure 4. UV-VIS-DR spectra of the samples supported on γ -Al₂O₃ (A), and MgO (B) as well as hydrotalcite-derived catalysts of HT20 (C) and HT40 (D) series.

The absorption band located at about 210 nm in a pure MgO spectrum (Figure 4B) is assigned to the excitation of five coordinated oxygen anions from the periclase structure [35]. The absorption peak around 295 nm and the shoulder at approximately 235 nm are

usually assigned to the excitation of defect states, which belong to O^{2-} surface anions at the edges and corners of the MgO nanocrystals [36]. In a spectrum of Ni-M, the absorption band around 390 nm and the shoulder around 635 nm are assigned to octahedrally coordinated Ni^{2+} cations in Ni-oxides [32].

The spectra recorded for the calcined Mg-Al hydrotalcites (HT20 and HT40 in Figure 4C,D) are characterised by a small peak at about 200 nm related to the excitation of five coordinated oxygen anions from the periclase structure [35]. Periclase was identified as the dominant phase formed from the thermal decomposition of hydrotalcite (Figure 2B). The spectra obtained for the calcined Ni-Mg-Al hydrotalcites, Ni-HT20 and Ni-HT40, show intense bands at 205–210 nm with a shoulder at about 235–250 nm, which possibly indicates the presence of defects related to O^{2-} surface anions at the edges and corners of the MgO nanocrystals [36]. Thus, thermal decomposition of Ni-Mg-Al hydrotalcite results in a more defected periclase in comparison to the decomposition of Mg-Al hydrotalcite. The broad bands at around 400 nm and a shoulder around 650 nm are assigned to octahedrally coordinated Ni^{2+} cations in Ni-oxides [32].

The Co-A spectrum consists of three not-fully-resolved maxima centred at about 275, 405 and 675 nm (Figure 4A). The first band is related to the alumina support; however, in this range, the band assigned to the $O^{2-} \rightarrow Co^{2+}$ charge transition could also be expected [37]. The bands at around 405 and 675 nm are related to coordination-metal charge transfer between $O^{2-} \rightarrow Co^{2+}$ and $O^{2-} \rightarrow Co^{3+}$ in Co_3O_4 , respectively [20]. The presence of a $CoAl_2O_4$ spinel phase also cannot be excluded in this case. Similar bands were identified for the Co-M sample; however, peaks at about 405 and 670 nm, assigned to the presence of Co_3O_4 spinel, are significantly less intense (Figure 4B). On the other hand, the broad band at about 225 nm is a superposition of the bands assigned to MgO and to the $O^{2-} \rightarrow Co^{2+}$ charge transition [37]. Thus, in the Co-M sample, the contribution of the Co_3O_4 spinel is lower compared to that of the Co-A catalyst.

The spectra recorded for Co-Mg-Al hydrotalcite-derived samples are characterised by a broad maximum centred at about 275–285 nm with a shoulder around 400 nm and a band centred at about 675 nm (Figure 4C,D). The first peak is a superposition of the bands characteristic of the periclase and the $O^{2-} \rightarrow Co^{2+}$ charge transition [35,37], while the bands around 400 and 675 nm are assigned to the coordination-metal charge transfer between $O^{2-} \rightarrow Co^{2+}$ and $O^{2-} \rightarrow Co^{3+}$ in Co_3O_4 , respectively [20].

The spectrum of the bimetallic CoNi-A sample is very complex (Figure 4A). The band around 260–280 nm is related to the alumina support, but in this range, the band indicating the $O^{2-} \rightarrow Co^{2+}$ charge transition could also be present [37]. At higher wavelength values, spectrum analysis is difficult and very speculative; however, it seems that the broad band centred at about 450–490 nm is related to coordination-metal charge transfer between $O^{2-} \rightarrow Co^{2+}$ in Co_3O_4 , while an increase in the light absorption above 550 nm is related to the $O^{2-} \rightarrow Co^{3+}$ charge transfer in Co_3O_4 [20]. The bands related to charge transitions in Co_3O_4 probably overlap with the band corresponding to the tetrahedral Ni^{2+} cations in the $NiAl_2O_4$ and $NiCo_2O_4$ spinels, which are expected to be located at about 600 nm, as well as with the d-d transition in octahedral coordinated Ni^{2+} (expected at about 630–650 nm) [30–32].

The spectrum recorded for CoNi-M is very similar to the spectrum of Co-M (Figure 4B). The broad maximum below 350 nm is a superposition of bands related to the excitation of the defect states of O^{2-} surface anions on the edges and corners of the MgO nanocrystals and of the band indicating the $O^{2-} \rightarrow Co^{2+}$ charge transition in cobalt oxide species [37]. The shoulder at about 380–560 nm is possibly a superposition of the band related to charge transfer between $O^{2-} \rightarrow Co^{2+}$ in Co_3O_4 and that related to the octahedrally coordinated Ni^{2+} cations in Ni-oxide species, while the shoulder above 600 nm is assigned to the $O^{2-} \rightarrow Co^{3+}$ charge transfer in Co_3O_4 overlapping with the band associated with the presence of octahedrally coordinated Ni^{2+} cations [20,30–34]. The spectra recorded for CoNi-HT20 (Figure 4C) and CoNi-HT40 (Figure 4D) are very similar to the CoNi-M spectrum (Figure 4B), and the bands present in these spectra are assigned in the same way.

Figure 5 presents the results of the temperature-programmed reduction of the samples, with hydrogen used as a reducing agent (H₂-TPR). The reduction profile of the Ni-M sample consists of complex low-temperature maxima with a main peak at about 520 °C and a high temperature maximum above 900 °C (Figure 5A). The low-temperature peaks are attributed to NiO species dispersed on MgO but weakly interacting with the support surface [38]. On the other hand, interaction of nickel with MgO may result in the formation of a Ni_{1-x}Mg_xO solid solution in which the reduction of Ni²⁺ is possible above 700 °C [38,39].

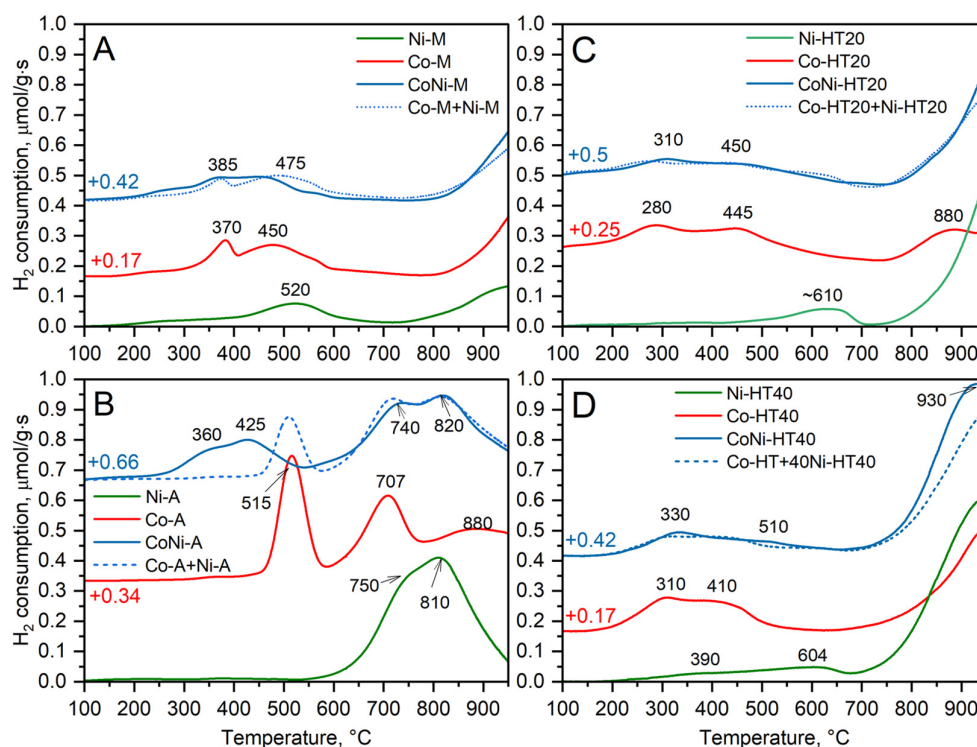


Figure 5. TPR profiles of the samples supported on γ -Al₂O₃ (A), and MgO (B) as well as for HT20 (C) and HT40 (D) series of the samples.

The reduction of nickel species in the Ni-A sample started at about 550 °C and is represented by a double reduction peak with maximums at 750 and 810 °C (Figure 5B), indicating stable nickel-oxide species. Such a stabilisation effect of nickel-oxide species deposited on alumina has been reported by many authors, including He et al. [40] and Wu et al. [41], who reported the formation of stable surface NiAl₂O₄ spinels under calcination conditions. Tillmann et al. [42] demonstrated that nickel in NiAl₂O₄ spinels deposited on alumina was reduced at about 800 °C. It should be noted that the spinel phase was identified in the Ni-A sample by XRD measurement (Figure 1A).

In the case of the Ni-HT20 and Ni-HT40 samples, only small amounts of Ni²⁺ cations, possibly in the form of NiO aggregates that interact relatively easily with a magnesia-alumina matrix, were reduced below 650 °C (Figure 5C,D). Most nickel-oxide species are reduced at temperatures above 700 °C. It indicates that nickel cations were incorporated into the Mg-Al-O matrix with the formation of mixed phases, such as Mg_xNi_{1-x}O and Mg_(1-y)Ni_yAl₂O₄. Reduction of Ni²⁺ cations in such mixed phases occurs at relatively high temperatures. Villa et al. [43] reported two reduction peaks centred at 720 and 1000 °C indicating the reduction of nickel cations in Mg_xNi_{1-x}O and Mg_(1-y)Ni_yAl₂O₄, respectively. Similarly, Apuzzo et al. [38] demonstrated that the reduction of Ni²⁺ cations in mixed

phases with MgO and Al₂O₃ occurred in the higher temperature range and was not completed at 900 °C.

The reduction of cobalt species in the Co-M sample occurred in several steps (Figure 5A). The peak at about 380 °C is related to the reduction of Co³⁺ to Co²⁺ in the Co₃O₄ spinel, which weakly interacts with MgO, while the maximum at about 480 °C is possibly related to the reduction of Co³⁺ to Co²⁺ in the Co₃O₄ and MgCo₂O₄ spinels interacting with the support surface [44]. Reduction of Co²⁺ to Co⁰ in CoO and Co_xMg_{1-x}O occurred above 700 °C [44]. It should be noted that both CoO and spinel phases were identified by XRD analysis of the Co-M sample (Figure 1B).

In the case of the Co-A sample, the reduction of Co³⁺ to Co²⁺ in Co₃O₄ is possibly represented by a peak at approximately 515 °C (Figure 5B). It should be noted that the reduction of cobalt in Co₃O₄ deposited on Al₂O₃ occurred at a significantly higher temperature than in the case of Co₃O₄ on MgO (Figure 5A). Thus, it seems that the interaction of cobalt spinel species with alumina is stronger than that with magnesium oxide. The reduction of Co²⁺ to Co⁰ in CoO, as well as in cobalt aluminates, takes place above 600 °C [45].

The low-temperature reduction maxima in TPR profiles of Co-HT20 (Figure 5C) and Co-HT40 (Figure 5D), which are located below 600 °C, are assigned to the reduction of Co³⁺ to Co²⁺ in cobalt aluminates, while the reduction of Co²⁺ to Co⁰ in CoO and cobalt aluminates takes place above 700 °C [45,46].

The reduction profiles of the hydrotalcite-derived bimetallic samples containing both nickel and cobalt, CoNi-HT20 and CoNi-HT40, are very similar to the superpositions of the monometallic samples, Co-HT20 + Ni-HT20 and Co-HT40 + Ni-HT40, respectively (Figure 5C,D). The profiles representing the superposition of the monometallic samples (dashed lines) were generated by adding suitable profiles of the Co- and Ni-containing samples with a 50% contribution from each of them. The reduction profile of the CoNi-M sample is shifted to lower temperatures of about 30–60 °C compared to the superposition of the Co-M + Ni-M profiles (Figure 5A). Furthermore, the decrease in the intensity of the peak located at about 450 °C in the case of the bimetallic sample indicates a lower contribution of cobalt in the Co₃O₄ and MgCo₂O₄ spinels interacting with the surface of MgO. The most significant differences were observed for the CoNi-A reduction profile and the superposition of the Co-A and Ni-A profiles (Figure 5B). In this case, the low-temperature reduction process of bimetallic samples took place at a temperature almost 200 °C lower than the first reduction peak from the sum of the reduction profiles of monometallic catalysts. The reduction profiles for bimetallic and monometallic samples above 550 °C are very similar. Therefore, the main differences are observed in the region characteristic of the Co³⁺-to-Co²⁺ reduction in Co-containing spinel phases. The explanation of these effects could be the possible formation of multicomponent spinels, such as Mg^{2+1-x-z}Ni^{2+x}Co^{2+z}Al^{3+2-y}Co^{3+y}O₄, with increased reducibility of Co³⁺ cations.

It should be noted that the reduction of the samples was not completed below 950 °C, indicating the presence of stable nickel and cobalt oxide species (Figure 5). The percentage contributions of the nickel and cobalt species reduced to the temperature 950 °C are presented in Table 2. Transition metal species deposited on alumina are significantly more effectively reduced by hydrogen than those deposited on magnesia. It is in line with the results obtained for hydrotalcite-derived materials. In samples with a higher aluminium content (HT40 series), the contribution of the transition metal in the reduced form is significantly higher compared to that in the samples with a lower aluminium content (HT20 series, Table 2). Thus, the support used significantly influenced the reducibility of the deposited transition-metal species.

Ammonia-desorption profiles obtained for the MgO, Al₂O₃ and hydrotalcite-derived Mg-Al oxide systems are compared in Figure 6. It was assumed that one ammonia molecule is chemisorbed at one acid site. Thus, the number of chemisorbed ammonia molecules is equal to the number of acid sites. All desorption profiles are spread in a relatively broad temperature range of 70–600 °C, indicating the presence of acid sites with the high

heterogeneity of their acidic strength. The profile obtained for MgO consists of a small number of low-intensity unresolved maxima, indicating a relatively low concentration of various types of surface acid sites ($30 \mu\text{mol/g}$). Ammonia desorption profiles obtained for other studied samples are significantly more intense, indicating a higher surface concentration of acid sites. The main maximum in the ammonia desorption profile of Al_2O_3 is located at about 170°C . Furthermore, for this sample, the shoulder at about $240\text{--}250^\circ\text{C}$ indicates the presence of stronger acid sites. The total number of acid sites determined for alumina is approximately $96 \mu\text{mol/g}$. Desorption profiles of both hydrotalcite-derived Mg-Al oxides, HT20 and HT40, are characterized by a similar shape but significantly differ with respect to their intensity (Figure 6). The main maxima are located at 170 and 185°C for HT20 and HT40, respectively, indicating slightly stronger acid sites in the sample with higher alumina content (HT40). Moreover, the shoulders at about $220\text{--}230$ and $310\text{--}320^\circ\text{C}$ indicate the presence of acid sites with stronger acidity. The number of acid sites for the samples with the higher aluminium content, HT40, is about $103 \mu\text{mol/g}$, while that in the sample with the lower aluminium content was estimated to be $67 \mu\text{mol/g}$. These differences are not surprising considering that alumina is responsible for the creation of acid sites.

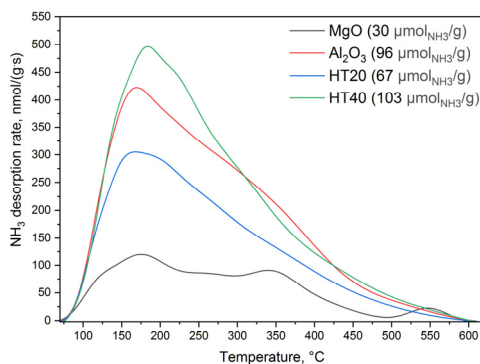


Figure 6. NH_3 -TPD profiles of the catalyst supports. Values of chemisorbed ammonia concentrations are shown in parentheses.

The results of the catalytic studies are shown in Figure 7. The reproducibility of the catalytic tests was verified in three subsequent runs. Differences in the obtained results are in the range of the error bars determined by the propagation-error method. In the case of ammonia decomposition to hydrogen and nitrogen over cobalt (Co-M) and nickel (Ni-M) deposited on MgO, the reaction started above 500°C and sharply increased reaching 90% of ammonia conversion at about $680\text{--}690^\circ\text{C}$ (Figure 7A). At temperatures below 600°C , Co-M showed higher ammonia conversion, while at higher temperatures, Ni-M was slightly more catalytically active. The bimetallic catalysts containing both cobalt and nickel (CoNi-M), with a total content of transition metals very similar to that of the monometallic samples, presented significantly improved catalytic activity. In this case, ammonia conversion started at about 455°C and 90% conversion was obtained at about 645°C . A similar effect was found for cobalt and nickel deposited on alumina (Figure 7B). Also, in this case, ammonia conversion measured in the presence of a monometallic catalyst was lower compared to that in the bimetallic sample. Ammonia decomposition started at about 425 and 445°C for the Co-A and Ni-A catalysts, respectively. Additionally, 90% ammonia conversion was obtained at 560°C for Co-A and 580°C for Ni-A. In the case of the bimetallic catalyst, CoNi-A, the reaction started at about 400°C ; however, at temperatures above 500°C , the conversion profiles of CoNi-A and Co-A are very similar (Figure 7B). Therefore, very significant differences in the activity of the catalysts were observed between the MgO and Al_2O_3 supports. Alumina is characterised by a significantly more acidic surface and therefore can more effectively adsorb ammonia molecules compared to

the more basic MgO (Figure 6). Pure alumina is not catalytically active in ammonia decomposition but may play the role of an ammonia reservoir for conversion over transition metals. Thus, one of the possible explanations for the better catalytic activity of the catalysts based on the alumina support could be its higher surface acidity in comparison to MgO-based catalysts. Of course, such differences in the ammonia-adsorption capacity can mainly be reflected in ammonia conversion at lower temperatures (ammonia was completely removed from the support surface at about 600 °C; Figure 6), an explanation that agrees with the results presented in Figures 6A,B.

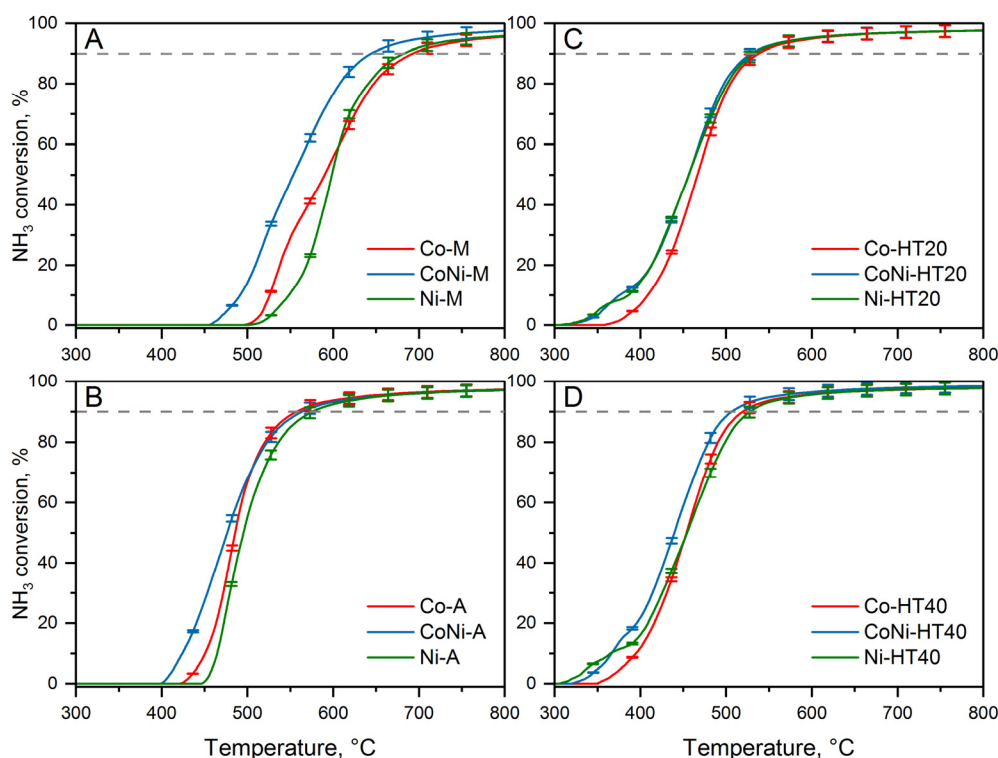


Figure 7. Results of catalytic NH_3 decomposition with error bars determined by the propagation error method over catalysts supported on MgO (A) and $\gamma\text{-Al}_2\text{O}_3$ (B), catalysts of HT20 (C) and HT40 (D) series. Dotted lines represent ammonia conversion of 90%.

Apart from significant differences in the ammonia-sorption capacities of Al_2O_3 and MgO, another important factor influencing the activities of various bimetallic catalysts could be the size of deposited transition crystallites and particles (Tables 1 and 2). In the case of the CoNi-A catalyst, the average size of transition-metal crystallites was about 10.4 nm, while for CoNi-M the average size was determined to be 20.6 nm. On the other hand, it is suggested that these crystallites aggregated, leading to the formation of significantly larger particles (Table 2). Assuming that active sites for ammonia decomposition are located on the surface of deposited and reduced transition-metal species, significantly more active sites are expected in the CoNi-A catalyst, which was found to be more catalytically active than CoNi-M. The ammonia decomposition over monometallic hydrotalcite-derived catalysts containing cobalt, Co-HT20 and Co-HT40, started at about 350 °C, and over these catalysts, 90% ammonia conversion was obtained at 540 and 520 °C, respectively (Figure 7C,D). In the case of the catalysts containing monometallic nickel, Ni-HT20 and Ni-HT40, as well as in the case of the bimetallic samples, CoNi-HT20 and CoNi-HT40, the reaction started at about 300–320 °C; 90% ammonia conversion was reached at 515 °C for Ni-HT20 and CoNi-HT20, at 525 °C for Ni-HT40 and at 505 °C for CoNi-HT40. Thus, hydrotalcite-derived catalysts presented significantly improved catalytic activity in

ammonia decomposition compared to supported catalysts based on cobalt and nickel deposited on magnesia or alumina (Figures 6A,B). The hydrotalcite-derived catalysts are characterised by a significantly higher specific surface area than either MgO or Al₂O₃ have (Table 1). The aluminium present in hydrotalcite-derived samples represents acid sites that can accumulate ammonia on the catalyst surface. As already postulated, such chemisorbed ammonia species could be a surface reservoir of this reactant. The comparison of the concentrations of chemisorbed ammonia, presented in Figure 6, shows the highest value for HT40 (103 μmol/g), while for HT20 and Al₂O₃, the surface ammonia concentrations were 67 and 96 μmol/g, respectively.

It seems that the reducibility of catalysts could play an important role in catalyst activation. The reduction process in the case of CoNi-A was initiated at a slightly lower temperature and proceeded with significantly higher intensity than did the process for CoNi-M (Figure 5A). Moreover, it started at significantly lower temperatures than the process for Co-A and Ni-A (Figure 5B). Moreover, it was shown that the contribution of reduced cobalt and nickel species in the samples based on an alumina support is significantly higher than those of samples based on an MgO support (Table 2). Similarly, in the case of the hydrotalcite-derived samples with higher aluminium content, the reduction of transition metals species was more effective compared to those with catalysts based on hydrotalcite-like samples with a lower aluminium content. Thus, assuming that reduced metal species play a role as catalytically active sites, the high reducibility of the catalysts is very important for catalyst activation.

To determine the catalytic activity of the individual active sites, the turnover frequency (TOF) values were determined for the selected most-active catalysts (Table 2). It was assumed that each reduced surface contained exposed metal atoms, as determined by pulse H₂ chemisorption (Table 2), which act as catalytically active sites. The highest TOF value was determined for the CoNi-A catalyst, with a value higher than that for the CoNi-M sample. The TOF values obtained for the hydrotalcite-derived catalysts were significantly lower than those for CoNi-A and CoNi-M. On the other side, the overall activity of the hydrotalcite-derived catalysts was better compared to that of other samples. However, it should be noted that the overall catalytic activity depends not only on the catalytic operation of the individual active site, but also on their surface concentration, which in the case of hydrotalcite-derived catalysts is significantly greater compared to those of other studied catalysts (Table 2).

A very important observation is the increased activity of bimetallic Co-Ni compared to those of monometallic catalysts containing nickel or cobalt. This problem was analysed by Tabassum et al. [12], who used Bader charge analysis to explain the synergistic cooperation of cobalt and nickel in ammonia decomposition. It was postulated that on the Co-Ni alloy surface, cobalt atoms are positively charged, whereas nickel atoms are negatively charged, resulting in the creation of localised charge polarisation. Such locally polarised sites are postulated to be more active in ammonia adsorption and dissociation. The suggested mechanisms of ammonia decomposition include its adsorption on the catalyst surface, N-H bond cleavage, retaliative fast recombination of hydrogen atoms and desorption of H₂ molecules, as well as re-combinative desorption of surface nitrogen atoms, which is the rate-determining step [12]. The recombination of surface-bonded nitrogen atoms to form an N₂ molecule requires the diffusion of such surface N atoms at the metal or alloy surface. This step requires that the atoms overcome a significantly high activation-energy barrier. Tabassum et al. [12] postulated that the more energetically favourable is the diffusion of N atoms toward the metal-oxide (support) interface followed by the recombination and desorption of the N₂ molecule. Such a positive effect of the catalytic support was shown for the Co-Ni alloy deposited on CeO₂ and MgO [12]. The nitrogen recombination rate is also related to the size of the metal or alloy species dispersed on the support surface. In the case of small metal or alloy aggregates deposited on the support surface, the contribution of the metal-support interface is greater compared to those of bulkier aggregates, and therefore, the recombination rate of N atoms should be faster. Thus, the

role of the support, as well as that of the dispersion of the catalytically active metals, is very important, as was shown also in the presented studies.

Fu et al. [13] and Li et al. [14] analysed the influence of the strength of the metal-ammonia bond ($M-NH_3$) on the efficiency of the ammonia decomposition to hydrogen and nitrogen. In the case of a too-weak $M-NH_3$ bond, desorption of ammonia is more likely than its dehydrogenation. On the other hand, if the $M-N$ bond energy is too high, the desorption of N-species from the catalyst surface becomes difficult. Therefore, metals that are able to create a moderately strong $M-N$ bond are favourable for catalytic ammonia decomposition. Hansgen et al. [47] calculated that the binding energy of $M-N$ necessary for the effective dissociative adsorption of NH_3 and the recombination and desorption of N_2 molecules should be approximately 134 kcal/mol, while for nickel and cobalt, these binding energies are 125 and 122 kcal/mol, respectively. Thus, in the case of these metals, the $M-N$ binding energies are too weak for effective decomposition of ammonia. On the other hand, Fu et al. [13] showed that the Co-Ni metal system is characterised by a moderately strong $M-N$ interaction, which is suitable for effective ammonia decomposition. Similarly, Wu et al. [15] compared the ammonia and nitrogen desorption profiles for nickel, cobalt and bimetallic Co-Ni systems deposited on silica. It was shown that both Ni and Co have $M-N$ binding energies that are too weak to be suitable for the effective dissociative adsorption of ammonia. However, bimetallic Ni-Co/ SiO_2 catalysts were characterised by moderate $M-N$ binding energy, which is suitable for dissociative adsorption of ammonia, recombination of N atoms and desorption of N_2 .

For the selected catalyst, CoNi-HT20, an additional isothermal stability test was conducted at 500 °C (Figure 8). The test showed a decrease in ammonia conversion of less than 1% during the 12-h stability test, which seems to be a very good and promising result.

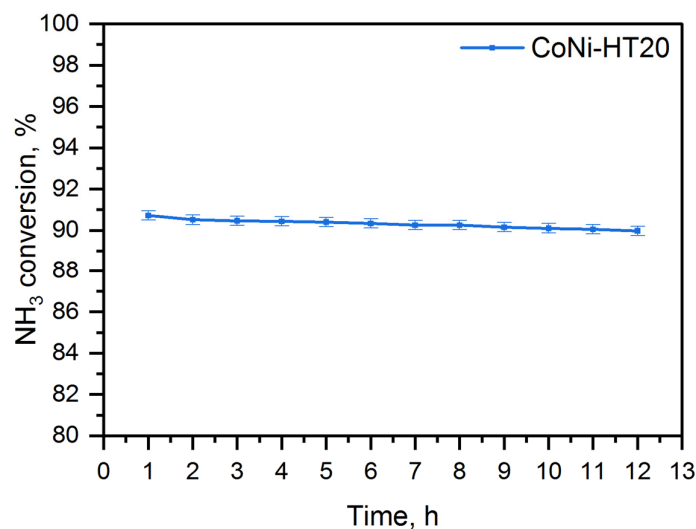


Figure 8. Isothermal catalytic stability test at 500 °C, with error bars determined by the propagation-error method.

4. Conclusions

Cobalt and nickel deposited on MgO and Al_2O_3 , as well as cobalt and nickel incorporated into the hydrotalcite-derived Mg-Al oxide matrix, were studied as catalysts for ammonia's decomposition to hydrogen and nitrogen. Cobalt and nickel deposited on a more acidic support, Al_2O_3 , showed much better catalytic activity compared to cobalt and nickel deposited on more basic MgO . It was suggested that alumina, in contrast to MgO , could be a more effective surface reservoir for the conversion of ammonia on transition-metal species. Moreover, transition metals deposited on alumina were more effectively reduced,

and therefore, more catalytically active sites were formed on alumina than on magnesia. Another suggested explanation for the higher activity of cobalt and nickel deposited on Al_2O_3 is the significantly smaller size of the transition-metal aggregates deposited on alumina in comparison to MgO , which led to the higher dispersion of catalytically active components. In the case of Al_2O_3 -based catalysts, the larger number of active sites for the effective dissociative adsorption of ammonia molecules, as well as the availability of more metal-support interfaces responsible for effective and fast nitrogen-atom recombination to N_2 , are expected. In both series of the supported catalysts, the best results were obtained using bimetallic Co-Ni catalysts. This effect was attributed to the more appropriate binding energy between the metal and the nitrogen atom of ammonia molecule, M-NH_3 , in the bimetallic Co-Ni system than in the monometallic Co or Ni catalysts, in which this binding energy is postulated to be too low, making cleavage of the M-N bond less effective.

The hydrotalcite-derived catalysts containing cobalt and nickel presented significantly better activity compared to the supported catalysts. In this case, the catalytic activity of individual active sites is lower, but the dispersion of transition metals in the Mg-Al oxide matrix is significantly higher than in Al_2O_3 - and MgO -based catalysts. The effect of the synergistic cooperation of Co and Ni was less evident in this series of catalysts. However, the positive effect of the increased surface acidity of the Mg-Al oxide matrix was identified. The catalysts with the higher Al/Mg ratio presented improved activity in comparison to the catalysts with the lower alumina content. The bimetallic hydrotalcite-derived catalyst presented high stability under reaction conditions.

Author Contributions: Conceptualization, A.K. and L.C.; methodology, A.K.; investigation, A.K., M.R., S.G. and M.P.; writing—original draft preparation, L.C., A.K. and M.R.; writing—review and editing, L.C. and A.K.; visualization, A.K.; supervision, A.K.; project administration, A.K. All authors have read and agreed to the published version of the manuscript.

Funding: This research was funded by the National Science Centre, Poland: 2018/31/N/ST4/01470.

Data Availability Statement: Experimental data will be available for the request.

Acknowledgments: The studies were carried out in the frame of project 2018/31/N/ST4/01470 from the National Science Centre (Poland). The study was carried out using research infrastructure funded by the European Union in the framework of the Smart Growth Operational Programme, Measure 4.2; Grant No. POIR.04.02.00-00-D001/20, “ATOMIN 2.0—Center for materials research on ATOMIC scale for the INnovative economy”.

Conflicts of Interest: The authors declare no conflicts of interest.

References

1. Howarth, R.W.; Jacobson, M.Z. How green is blue hydrogen? *Energy Sci. Eng.* **2021**, *9*, 1676–1687. <https://doi.org/10.1002/ese3.956>.
2. Hren, R.; Vujanovic, A.; Van Fan, Y.; Klimes, J.J.; Krajnc, D.; Cucek, L.; Hydrogen production, storage and transport for renewable energy and chemicals: An environmental footprint assessment. *Renew. Sustain. Energy Rev.* **2023**, *173*, 113113. <https://doi.org/10.1016/j.rser.2022.113113>.
3. Qyyum, M.A.; Dickson, R.; Shah, S.F.A.; Niaz, H.; Khan, A.; Liu, J.J.; Lee, M. Availability, versatility, and viability of feedstocks for hydrogen production: Product space perspective. *Renew. Sustain. Energy Rev.* **2021**, *145*, 110843. <https://doi.org/10.1016/j.rser.2021.110843>.
4. Abdin, Z.; Zafaranloo, A.; Rafiee, A.; Mérida, W.; Lipiński, W.; Khalilpour, K.R. Hydrogen as an energy vector. *Renew. Sustain. Energy Rev.* **2020**, *120*, 109620. <https://doi.org/10.1016/j.rser.2019.109620>.
5. Akhtar, M.S.; Dickson, R.; Liu, J.J. Life cycle assessment of inland green hydrogen supply chain networks with current challenges and future prospects. *ACS Sustain. Chem. Eng.* **2021**, *9*, 17152–17163. <https://doi.org/10.1021/acssuschemeng.1c06769>.
6. Młotek, M.; Perron, M.; Krawczyk, K. Ammonia Decomposition in a Gliding Discharge Plasma. *Energy Technol.* **2021**, *9*, 2100677. <https://doi.org/10.1002/ente.202100677>.
7. Chatterjee, S.; Parsapur, R.K.; Huang, K.-W. Limitations of Ammonia as a Hydrogen Energy Carrier for the Transportation Sector. *ACS Energy Lett.* **2021**, *6*, 4390–4394. <https://doi.org/10.1021/acsenerylett.1c02189>.
8. Hu, Z.; Mahin, J.; Datta, S.; Bell, T.E.; Torrente-Murciano, L. Ru-Based Catalysts for H_2 Production from Ammonia: Effect of 1D Support. *Top. Catal.* **2019**, *62*, 1169–1177. <https://doi.org/10.1007/s11244-018-1058-3>.

9. Chen, C.; Wu, K.; Ren, H.; Zhou, C.; Luo, Y.; Lin, L.; Au, C.; Jiang, L. Ru-Based Catalysts for Ammonia Decomposition: A Mini-Review. *Energy Fuels* **2021**, *35*, 11693–11706. <https://doi.org/10.1021/acs.energyfuels.1c01261>.
10. Guo, J.; Chen, P. Interplay of Alkali, Transition Metals, Nitrogen, and Hydrogen in Ammonia Synthesis and Decomposition Reactions. *Acc. Chem. Res.* **2021**, *54*, 2434–2444. <https://doi.org/10.1021/acs.accounts.1c00076>.
11. Huang, C.; Yu, Y.; Yang, J.; Yan, Y.; Wang, D.; Hu, F.; Wang, X.; Zhang, R.; Feng, G. Ru/La₂O₃ catalyst for ammonia decomposition to hydrogen. *Appl. Surf. Sci.* **2019**, *476*, 928–936. <https://doi.org/10.1016/j.apsusc.2019.01.112>.
12. Tabassum, H.; Mukherjee, S.; Chen, J.; Holiharimanana, D.; Karakalos, S.; Yang, X.; Hwang, S.; Zhang, T.; Lu, B.; Chen, M.; et al. Hydrogen generation via ammonia decomposition on highly efficient and stable Ru-free catalysts: Approaching complete conversion at 450 °C. *Energy Environ. Sci.* **2022**, *15*, 4190–4200. <https://doi.org/10.1039/d1ee03730g>.
13. Fu, E.; Qiu, Y.; Lu, H.; Wang, S.; Liu, L.; Feng, H.; Yang, Y.; Wu, Z.; Xie, Y.; Gong, F.; et al. Enhanced NH₃ decomposition for H₂ production over bimetallic M(M = Co, Fe, Cu)Ni/Al₂O₃. *Fuel Process. Technol.* **2021**, *221*, 106945. <https://doi.org/10.1016/j.fuproc.2021.106945>.
14. Li, C.; Guo, L.; Chen, G.; Fu, Y.; Zhang, X.; Zou, Y.; Duan, J.; Wang, W. CoNi alloy catalyst supported on Zr-modified Y₂O₃ for ammonia decomposition to CO_x-free hydrogen. *Colloids Surf. A Physicochem. Eng. Asp.* **2023**, *671*, 131671. <https://doi.org/10.1016/j.colsurfa.2023.131671>.
15. Wu, Z.-W.; Li, X.; Qin, Y.-H.; Deng, L.; Wang, C.-W.; Jiang, X. Ammonia decomposition over SiO₂-supported Ni-Co bimetallic catalyst for CO_x-free hydrogen generation. *Int. J. Hydrogen Energy* **2020**, *45*, 15263–15269. <https://doi.org/10.1016/j.ijhydene.2020.04.007>.
16. Lucentini, I.; Garcia, X.; Vendrell, X.; Llorca, J. Review of the Decomposition of Ammonia to Generate Hydrogen. *Ind. Eng. Chem. Res.* **2021**, *60*, 18560–18611. <https://doi.org/10.1021/acs.iecr.1c00843>.
17. Huo, L.; Liu, B.; Li, H.; Cao, B.; Hu, X.-C.; Fu, X.-P.; Jia, C.; Zhang, J. Component synergy and armor protection induced superior catalytic activity and stability of ultrathin Co-Fe spinel nanosheets confined in mesoporous silica shells for ammonia decomposition reaction. *Appl. Catal. B* **2019**, *253*, 121–130. <https://doi.org/10.1016/j.apcatb.2019.04.053>.
18. Mohammed, A.A.; Khodair, Z.T.; Khadom, A.A. Preparation and investigation of the structural properties of α-Al₂O₃ nanoparticles using the sol-gel method. *Chem. Data Collect.* **2020**, *29*, 100531. <https://doi.org/10.1016/j.cdc.2020.100531>.
19. Safaei-Ghomia, J.; Zahedia, S.; Javida, M.; Ghasemzadeh, M.A. MgO Nanoparticles: An Efficient, Green and Reusable Catalyst for the One-pot Syntheses of 2,6-Dicyanoanilines and 1,3-Diarylpropyl Malononitriles under Different Conditions. *J. Nanostruct.* **2015**, *5*, 153–160. <https://doi.org/10.7508/jns.2015.02.010>.
20. Zhao, Z.; Wang, Z.; Tong, Y.; Sun, J.; Ke, M.; Song, W. Al₂O₃ Nanorod with Rich Pentacoordinate Al³⁺ Sites Stabilizing Co²⁺ for Propane Dehydrogenation. *Catalysts* **2023**, *13*, 807. <https://doi.org/10.3390/catal13050807>.
21. Sharma, J.K.; Srivastava, P.; Singh, G.; Akhtar, M.S.; Ameen, S. Green synthesis of Co₃O₄ nanoparticles and their applications in thermal decomposition of ammonium perchlorate and dye-sensitized solar cells. *Mater. Sci. Eng. B.* **2015**, *193*, 181–188. <https://doi.org/10.1016/j.mseb.2014.12.012>.
22. Riani, P.; Spennati, E.; Garcia, M.V.; Escribano, V.S.; Busca, G.; Garbarino, G. Ni/Al₂O₃ catalysts for CO₂ methanation: Effect of silica and nickel loading. *Int. J. Hydrogen Energy* **2023**, *48*, 24976–24995. <https://doi.org/10.1016/j.ijhydene.2023.01.002>.
23. Jayaseelan, C.; Rahuman, A.A.; Ramkumar, R.; Perumal, P.; Rajakumar, G.; Kirthi, A.V.; Santhoshkumar, T.; Marimuthu, S. Effect of sub-acute exposure to nickel nanoparticles on oxidative stress and histopathological changes in Mozambique tilapia, *Oreochromis mossambicus*. *Ecotoxicol. Environ. Saf.* **2014**, *107*, 220–228. <https://doi.org/10.1016/j.ecoenv.2014.06.012>.
24. Khe, C.; Aziz, A.; Lockman, Z. Synthesis of Cobalt/Gold Bimetallic Particles with Porous Flake-Like Nanostructures and Their Magnetic Properties. *Nanosci. Nanotechnol. Lett.* **2012**, *4*, 687–692. <https://doi.org/10.1166/nnl.2012.1390>.
25. Basąg, S.; Piwowarska, Z.; Kowalczyk, A.; Węgrzyn, A.; Baran, R.; Gil, B.; Michalik, M.; Chmielarz, L. Cu-Mg-Al hydrotalcite-like materials as precursors of effective catalysts for selective oxidation of ammonia to dinitrogen—The influence of Mg/Al ratio and calcination temperature. *Appl. Clay Sci.* **2016**, *129*, 122–130. <https://doi.org/10.1016/j.clay.2016.05.019>.
26. Chmielarz, L.; Jabłońska, M.; Strumiński, A.; Piwowarska, Z.; Węgrzyn, A.; Witkowski, S.; Michalik, M. Selective Catalytic Oxidation of Ammonia to Nitrogen over Mg-Al, Cu-Mg-Al and Fe-Mg-Al Mixed Metal Oxides Doped with Noble Metals. *Appl. Catal. B* **2013**, *130–131*, 152–162. <https://doi.org/10.1016/j.apcatb.2012.11.004>.
27. Wei, Z.; Qiao, H.; Yang, H.; Zhang, C.; Yan, X. Characterization of NiO nanoparticles by anodic arc plasma method. *J. Alloys Compd.* **2009**, *479*, 855–858. <https://doi.org/10.1016/j.jallcom.2009.01.064>.
28. Belles, L.; Moularas, C.; Smykała, S.; Deligiannakis, Y. Flame Spray Pyrolysis Co₃O₄/CoO as Highly-Efficient Nanocatalyst for Oxygen Reduction Reaction. *Nanomaterials* **2021**, *11*, 925. <https://doi.org/10.3390/nano11040925>.
29. Pérez Osorio, G.; Fuentes Moyado, S.; Petranovskii, V.; Simakov, A. PdO/Al₂O₃-(Ce_{1-x}Zr_x)O₂ catalysts: Effect of the sol-gel support composition. *Catal. Lett.* **2006**, *110*, 53–60. <https://doi.org/10.1007/s10562-006-0097-8>.
30. Sengupta, S.; Ray, K.; Deo, G. Effects of modifying Ni/Al₂O₃ catalyst with cobalt on the reforming of CH₄ with CO₂ and cracking of CH₄ reactions. *Int. J. Hydrogen Energy* **2014**, *39*, 11462–11472. <https://doi.org/10.1016/j.ijhydene.2014.05.058>.
31. Weber, S.; Abel, K.L.; Zimmermann, R.T.; Huang, X.; Bremer, J.; Rihko-Struckmann, L.K.; Batey, D.; Cipiccia, S.; Titus, J.; Poppitz, D.; et al. Porosity and Structure of Hierarchically Porous Ni/Al₂O₃ Catalysts for CO₂ Methanation. *Catalysts* **2020**, *10*, 1471. <https://doi.org/10.3390/catal10121471>.
32. Gonzalez, C.J.; Boukha, Z.; Rivas, B.D.; Delgado, J.J.; Cauqui, M.A.; Velasco, J.R.G.; Ortiz, J.I.G.; Fonseca, R.L. Structural characterisation of Ni/alumina reforming catalysts activated at high temperatures. *Appl. Catal. A Gen.* **2013**, *466*, 9–20. <https://doi.org/10.1016/j.apcata.2013.06.017>.

33. Kathiraser, Y.; Thitsartarn, W.; Sutthiumporn, K.; Kawi, S. Inverse NiAl₂O₄ on LaAlO₃–Al₂O₃: Unique Catalytic Structure for Stable CO₂ Reforming of Methane. *J. Phys. Chem. C* **2013**, *117*, 8120–8130. <https://doi.org/10.1021/jp401855x>.
34. Zhang, L.; Wang, X.; Chen, C.; Zou, X.; Shang, X.; Ding, W.; Lu, X. Investigation of mesoporous NiAl₂O₄/MO_x (M = La, Ce, Ca, Mg)–γ-Al₂O₃ nanocomposites for dry reforming of methane. *RSC Adv.* **2017**, *7*, 33143. <https://doi.org/10.1039/c7ra04497f>.
35. Todan, L.; Predoana, L.; Petcu, G.; Preda, S.; Culiță, D.C.; Baran, A.; Trus, R.-D.; Surdu, V.-A.; Vasile, B.S.; Ianculescu, A.-C. Comparative Study of MgO Nanopowders Prepared by Different Chemical Methods. *Gels* **2023**, *9*, 624. <https://doi.org/10.3390/gels9080624>.
36. Stankic, S.; Sterrer, M.; Hofmann, P.; Bernardi, J.; Diwald, O.; Knözinger, E. Novel Optical Surface Properties of Ca²⁺-Doped MgO Nanocrystals. *Nano Lett.* **2005**, *5*, 1889. <https://doi.org/10.1021/nl0511418>.
37. Abdallah, A.M.; Awad, R. Study of the Structural and Physical Properties of Co₃O₄ Nanoparticles Synthesized by Co-Precipitation Method. *J. Supercond. Nov. Magn.* **2020**, *33*, 1395–1404. <https://doi.org/10.1007/s10948-019-05296-1>.
38. Apuzzo, J.; Cimino, S.; Lisi, L. Ni or Ru supported on MgO/γ-Al₂O₃ pellets for the catalytic conversion of ethanol into butanol. *RSC Adv.* **2018**, *8*, 25846. <https://doi.org/10.1039/c8ra04310h>.
39. Parmaliana, A.; Arena, F.; Frusteri, F.; Giordano, Temperature-programmed reduction study of NiO–MgO interactions in magnesia-supported Ni catalysts and NiO–MgO physical mixture. *N. J. Chem. Soc. Faraday Trans.* **1990**, *86*, 2663–2669. <https://doi.org/10.1039/FT9908602663>.
40. He, L.; Ren, Y.; Yue, B.; Tsang, S.C.E.; He, H. Tuning Metal–Support Interactions on Ni/Al₂O₃ Catalysts to Improve Catalytic Activity and Stability for Dry Reforming of Methane. *Processes* **2021**, *9*, 706. <https://doi.org/10.3390/pr9040706>.
41. Wu, J.; Ren, S.; Zhao, R.; Wang, Z.; Lei, Z.; Kang, S.; Pan, C.; Li, Z.; Yan, J.; Shui, H. Promotion of the Ni/γ-Al₂O₃ catalyst for the hydrogenation of naphthalene by silica coating. *React. Kinet. Mech. Catal.* **2019**, *128*, 793–807. <https://doi.org/10.1007/s11144-019-01651-4>.
42. Tillmann, L.; Schulwitz, J.; Veen, A.; Muhler, M. Dry Reforming of Methane at High Pressure in a Fixed-Bed Reactor with Axial Temperature Profile Determination. *Catal. Lett.* **2018**, *148*, 2256–2262. <https://doi.org/10.1007/s10562-018-2453-x>.
43. Villa, R.; Cristiani, C.; Groppi, G.; Lietti, L.; Forzatti, P.; Cornaro, U.; Rossini, S. Ni based mixed oxide materials for CH₄ oxidation under redox cycle conditions. *J. Mol. Catal. A Chem.* **2003**, *204–205*, 637–646. [https://doi.org/10.1016/S1381-1169\(03\)00346-7](https://doi.org/10.1016/S1381-1169(03)00346-7).
44. Awadallah, A.E.; Abdel-Mottaleb, M.S.; Aboul-Enein, A.A.; Yonis, M.M.; Aboul-Gheit, A.K. Catalytic Decomposition of Natural Gas to CO/CO₂–Free Hydrogen Production and Carbon Nanomaterials Using MgO-Supported Monometallic Iron Family Catalysts. *Chem. Eng. Commun.* **2015**, *202*, 163–174. <https://doi.org/10.1080/00986445.2013.836631>.
45. Lu, M.; Fatah, N.; Khodakov, A.Y. Optimization of solvent-free mechanochemical synthesis of Co/Al₂O₃ catalysts using low- and high-energy processes. *J. Mater. Sci.* **2017**, *52*, 12031–12043. <https://doi.org/10.1007/s10853-017-1299-8>.
46. Fatah, N.; Dhainaut, F. Analysis of particle breakage during the preparation steps of Co/Al₂O₃ catalysts. *J. Mater. Sci.* **2019**, *54*, 14275–14286. <https://doi.org/10.1007/s10853-019-03918-6>.
47. Hansgen, D.A.; Vlachos, D.G.; Chen, J.G. Using first principles to predict bimetallic catalysts for the ammonia decomposition reaction. *Nat. Chem.* **2010**, *2*, 484–489. <https://doi.org/10.1038/nchem.626>.

Disclaimer/Publisher’s Note: The statements, opinions and data contained in all publications are solely those of the individual author(s) and contributor(s) and not of MDPI and/or the editor(s). MDPI and/or the editor(s) disclaim responsibility for any injury to people or property resulting from any ideas, methods, instructions or products referred to in the content.